Supplemental Material

for

Electron spin contrast of Purcell-enhanced nitrogen-vacancy ensembles in nanodiamonds

1. Sample preparation

The 200-nm thick TiN films used in this work were grown on c-sapphire substrates (GT Crystal Systems, LLC, USA) using DC reactive magnetron sputtering. The deposition was performed in Ar-N_2 atmosphere with a pressure of 5mTorr and gas flow rates of Ar and N_2 being 4 and 6 sccm, respectively. During the deposition, the substrates were maintained at 800ºC and the deposition rate was kept at approximately 2 nm/min. The TiN is expected to have epitaxial <111> orientation structure, as has been demonstrated in previous work [S1].

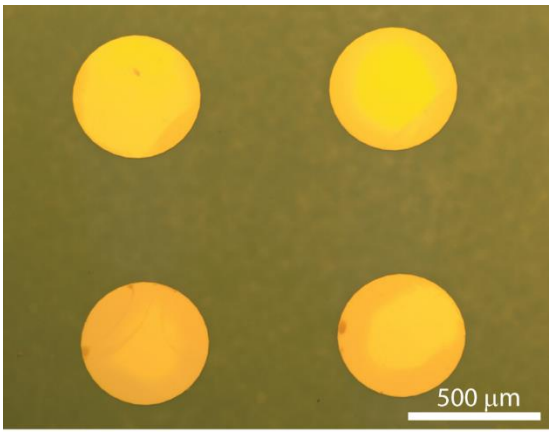

Supplementary Figure 1. Optical microscope image of TiN islands grown on a c-axis sapphire. The islands are 200 nm thick and 500 μm in diameter.

The TiN film was patterned into islands, each 500 μm in diameter (see Supplementary Figure 1). Islands were fabricated using photolithography (photoresist AZ 5214 in image reversal mode) followed by inductively coupled plasma (ICP) reactive ion etching using chlorine gas.

2. Spread of nanodiamond size

The nanodiamonds (NDs) used in this experiment were purchased in the form of an aqueous suspension of 0.1% w/v (1mg/mL) from Adamas Nanotechnologies, Inc. Per the manufacturer specifications, the average size of the nanodiamonds is 100 nm and each nanocrystal contains approximately 400 NV centers.

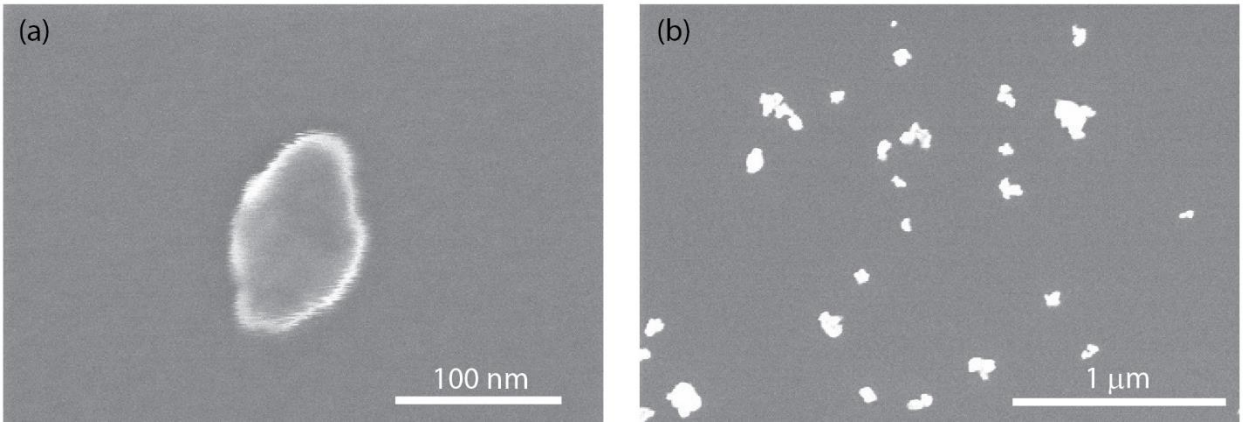

Supplementary Figure 2. Illustrative SEM scans of nanodiamonds on Si substrate: (a) zoomed-in scan of a typical nanodiamond and (b) overview of available nanocrystals. The average nanodiamond size is (76±21) nm. The average values are calculated from 22 measured nanodiamonds.

We analyzed the ND size statistics by using scanning electron microscopy of the NDs spin-coated on top of Si substrate. For the 22 examined nanocrystals, the average size was 76 nm with standard deviation of 21 nm. Supplementary Figure 2 shows the SEM scans of nanodiamonds dispersed on a Si substrate. As determined by confocal fluorescence mapping, the concentration of nanodiamonds on the sample used in the experiment was on the order of 0.1 μm^{-2}.

3. NVE characterization setup

For the fluorescence lifetime measurements, the nanodiamond-based NV centers were optically pumped with a 532nm, 100-ps pulsed laser (PicoQuant; LDH-P-FA-530L) at a 2.5 MHz repetition rate. Both the laser excitation and photoluminescence signal collection used the same oil-immersion objective lens (Nikon; CFI Apo TIRF 100X Oil) with a numerical aperture of 1.49 (Supplementary Figure 3). The collected signal was sent through a 50-μm confocal aperture and

filtered using a dichroic mirror and a band-pass filter (650-720 nm) to suppress the pump photons. The photon counting was performed by a single-photon avalanche photodiode (SPAD, PerkinElmer; SPCM–AQRH–14–FC) connected to an electronic correlation module (PicoQuant; TimeHarp 200). For the spin contrast measurements, we have used a 532 nm CW laser (SLOC, GL532NA-200) modulated with an acousto-optical modulator (AOM, Gooch & Housego, 1350AF-DIFO-1.0) to produce 15 μs pulses. A pulse counter (Measurement Computing, USB-CTR04 series) was used for counting the electrical pulses from the SPAD. For the optically detected magnetic resonance (ODMR) measurements, the microwave signal at frequencies between 2.84 and 2.90 GHz was generated by an Agilent E8254A generator, modulated by a Mini-Circuits ZASW-2-50DR+ switch and amplified by a 16 W Mini-Circuits ZHL-16W-43 RF amplifier. The AOM, the counter, and the microwave switch were gated using a delay generator (DG645, Stanford Research Instruments) to produce sequences for T_1-contrast and ODMR lock-in measurements.

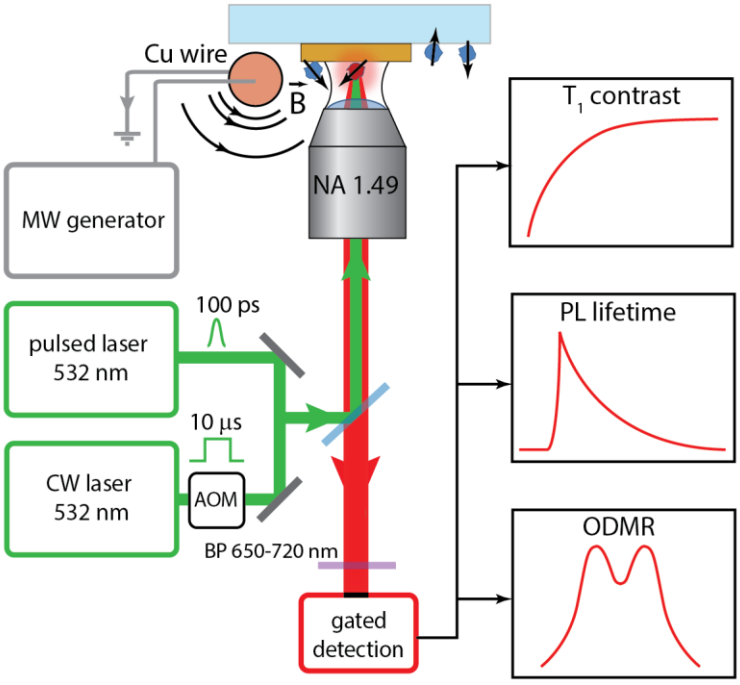

Supplementary Figure 3. Schematic of the experimental setup comprising a pulsed laser for TCSPC measurements, a modulated CW laser for spin contrast measurements, a high NA oil immersion objective for pump delivery and fluorescence collection, a microwave excitation source for ODMR measurements, and a gated detection module.

4. NVE fluorescence lifetime statistics

The fluorescence lifetime was retrieved by fitting the decay curves experimentally obtained by using the method of time-correlated single-photon counting (TCSPC) [S2]. The fluorescence TCSPC decay was fitted with a gamma-weighted integral of exponential decays convolved with the instrument response function (IRF). The average value of the resulting gamma distribution was considered to be the lifetime of the NVE. Figure 2(b) of the main text shows typical fluorescence decay curves for NVEs on sapphire and on TiN. To avoid bias towards measuring a shorter lifetime than the average lifetime of the NVE, the collection rates in this experiment were made much lower than the laser pulse repetition rate (<0.25 MHz and 2.5 MHz respectively). In this way, less than one NV center per pulse was contributing to the TCSPC histogram.

The NVE was assumed to be gamma-distributed in fluorescence lifetime:

$$n_{\tau_{\mathrm{av}},b}(\tau) \sim (b\tau)^{b\tau_{\mathrm{av}}-1} e^{-b\tau} \tag{S1}$$

where $n_{\tau_{\mathrm{av}},\beta}(\tau)$ is the probability density for an NV center to have a lifetime τ, with $b = \tau_{\mathrm{av}}/\delta\tau^2$ (τ_{av} being the average lifetime of the NVE and $\delta\tau$ being the lifetime standard deviation). Both τ_{av} and $\delta\tau$ were used as fitting parameters. The IRF was measured by collecting the attenuated laser pulses using the same detector used for the TCSPC measurement. The TCSPC fitting function was the theoretical intensity emitted by an NVE after an instantaneous excitation convoluted with the IRF:

$$I_{\mathrm{fit}}(t) = \int_0^{\infty}\int_{-\infty}^{t} \frac{n_{\tau_{\mathrm{av}},b}(\tau)}{\tau} e^{(t'-t)/\tau}\,\mathrm{IRF}(t')dt'd\tau \tag{S2}$$

Collective spontaneous emission is not expected to significantly disturb the fluorescence lifetime measurement of NVE [S3]. Indeed, the superradiant decay time τ/N, where N = 1000 is the number of NV centers in a typical NVE, is several orders of magnitude larger than the decoherence time of NV fluorescence $\left(T_2^* \sim 1/\delta\omega\right)$, where $\delta\omega \sim 100$ Trad/s is the spectral width of NV emission.

5. Averaging fluorescence rate of NVE over different NV axes orientations

In this Section, we consider the effect of different NV axis orientations and random nanodiamond lattice orientation on the fluorescence rate of the NVE. We assume that the fluorescence lifetime of all the NV centers is equal to τ (the lifetime distribution is separately discussed in Supplementary Section 4). We show that the NVE fluorescence rate is well approximated by the fluorescence rate of a collection of single, identically oriented NVs. In all calculations in this Section, the fluorescence rates are normalized by N/τ, where N is the number of NV centers considered and $1/\tau$ is the maximum emission rate of an individual NV center.

We assume a linearly polarized excitation beam with power P_l exciting a nanodiamond NVE. Let us first consider a reference NV center whose axis is parallel to the optical axis. The absorption and emission dipoles of the NV center are then parallel to the electric field and the fluorescence rate of the reference NV is

$$f^{(\mathrm{r})} = \frac{k_{\mathrm{opt}}^{(\mathrm{r})}\tau}{1+k_{\mathrm{opt}}^{(\mathrm{r})}\tau} = \frac{s^{(\mathrm{r})}}{1+s^{(\mathrm{r})}} \ , \tag{S3}$$

where $k_{\mathrm{opt}}^{(r)} = c_{\mathrm{opt}}^{(r)} P_l$ and $c_{\mathrm{opt}}^{(r)}$ is a constant, which only depends on the absorption cross-section and fixed experimental parameters. We have also defined the pump saturation parameter $s^{(\mathrm{r})} = P_l c_{\mathrm{opt}}^{(\mathrm{r})}\tau$, which is a convenient dimensionless measure of pump intensity.

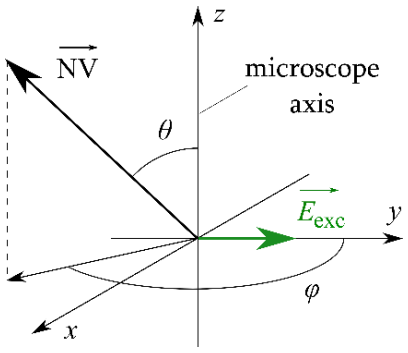

Supplementary Figure 4. Orientation of an NV center axis relative to the microscope optical axis (z) and the laser polarization axis (y) parametrized by angles θ and φ.

To calculate the fluorescence of a real NVE, we must account for the different NV axis orientations. We describe the axis orientation by the two angles θ and φ that the NV axis forms with the microscope axis and the laser polarization, respectively (see Supplementary Figure 4).

Now we define the excitation rate $k_{\mathrm{opt}}^{(i)}$ for the *i*-th NV center in the NVE. The absorption dipoles of the NV are perpendicular to its axis. Therefore, $k_{\mathrm{opt}}^{(i)}$ as a function of the axis orientation can be expressed as follows:

$$k_{\mathrm{opt}}^{(i)} = k_{\mathrm{opt}}^{(\mathrm{r})}\left(1-\sin^2\theta_i\cos^2\varphi_i\right) \tag{S4}$$

For each possible nanodiamond orientation (which is a priori random), there are 4 different NV axis orientations along the directions of chemical bonds in the diamond lattice. We calculate the NVE fluorescence saturation curve corresponding to an "average" nanodiamond lattice orientation (see the black data points in Supplementary Figure 5).

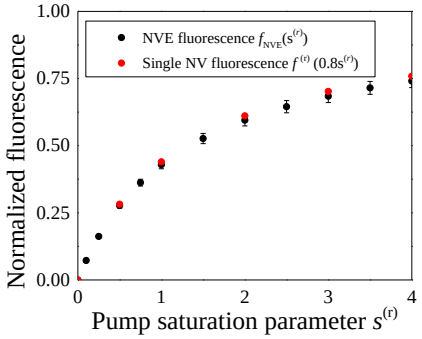

Supplementary Figure 5. The theoretical dependence of normalized NVE fluorescence f_{NVE} averaged over all the nanodiamond lattice orientations on the reference saturation parameter $s^{(\mathrm{r})} = k_{\mathrm{opt}}^{(\mathrm{r})}\tau$. The error bar represents standard deviations of f_{NVE} for varying nanodiamond lattice orientation (black). Single NV fluorescence rate (red) for a reduced pump power ($0.8s^{(\mathrm{r})}$), approximates well the NVE fluorescence rate.

The fluorescence from a nanodiamond NVE weakly depends on the nanodiamond orientation. We numerically show (see the red data points in Supplementary Figure 5) that its value can be well approximated by $f_{\mathrm{NVE}}(s^{(\mathrm{r})}) \approx f^{(\mathrm{r})}(0.8s^{(\mathrm{r})})$. Therefore, we can account for the NV orientations within a nanodiamond by defining the NVE optical excitation rate as $k_{\mathrm{opt}} = c_{\mathrm{opt}}P_l$, where $c_{\mathrm{opt}} = 0.8c_{\mathrm{opt}}^{(\mathrm{r})}$.

6. Calibration of optical excitation rate

We assume that the excitation rate k_{opt} is proportional to the laser power P_l through $k_{opt} = c_{opt} P_l$, where c_{opt} is the constant defined in Supplementary Section 5. Additionally, the theoretical photon emission rate $R(k_{opt})$ and the experimental count rate $I(P_l)$ are related by a constant efficiency parameter $\eta = I/R$. To calibrate the optical excitation rate k_{opt}, we measured the optical saturation curves for NVEs found on TiN and sapphire (see Supplementary Figure 6) as well as their fluorescence lifetime statistics. Using the kinetic model presented in the main text, we have simulated the expected dependence of the steady-state fluorescence rate from the NVE, while accounting for the distribution of lifetimes (see Supplementary Section 4) and axis (see Supplementary Section 5) orientations. By fitting c_{opt} and η we convert the measured laser power into the optical excitation rate of the NVE.

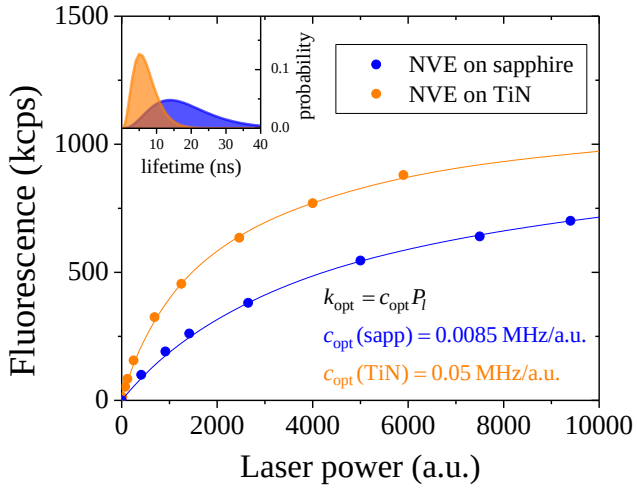

Supplementary Figure 6. Optical saturation curve of NVE fluorescence on sapphire and TiN as a function of laser power P_l. Inset: lifetime distributions of NV centers in the two NVEs deduced from the TCSPC decay curves.

The higher value of c_{opt} obtained on TiN suggests that the pump light is enhanced by the metallic substrate. Two effects may be responsible for this enhancement. The first effect is constructive interference between the incident and reflected waves. Secondly, the interface between the diamond and the substrate could support localized plasmons at the pump wavelength, causing the pump power density to be further enhanced.

7. Calculation of Purcell effect for NVEs on TiN film

To estimate the expected lifetime shortening caused by the TiN film, we numerically simulated the power emitted by an NV center situated at the center of a 76 nm spherical diameter nanodiamond in three different situations:

a. Nanodiamond in vacuum

In this situation, the emission rate of the NV center Γ_{ND} is similar to the emission rate Γ_0 for a vanishingly small nanodiamond. We found $\Gamma_{ND}/\Gamma_{bulk} = 0.075$, corresponding to a lifetime of 170 ns. We express the subsequent decay rates by normalizing them to Γ_{ND}.

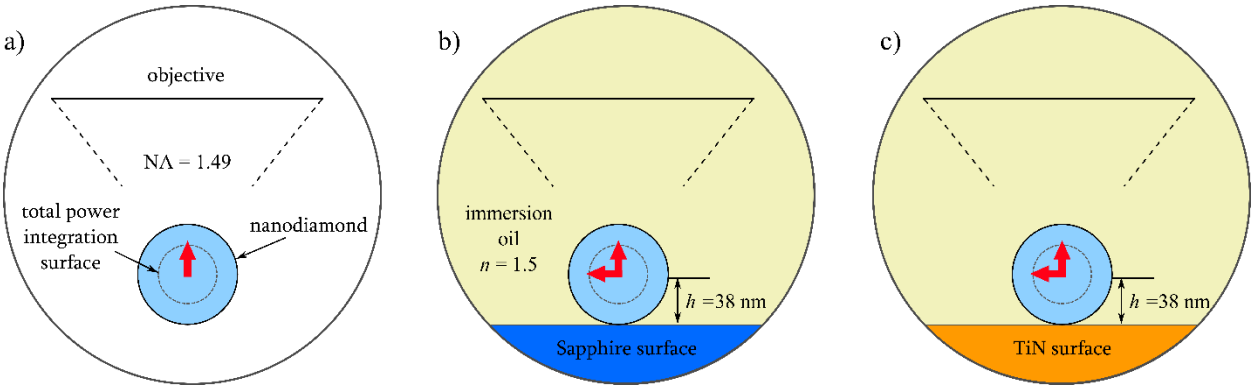

Supplementary Figure 7. Simulated configurations for estimating the lifetime decrease on a TiN substrate compared to a sapphire substrate (a) Nanodiamond in vacuum. (b) Nanodiamond on a sapphire surface. (c) Nanodiamond on a TiN surface. In all three cases, we consider NV centers placed at the nanodiamond center.

b. Nanodiamond on a sapphire substrate immersed in oil

The decay rate of the NV center in this geometry depends on the dipole orientation. For an in-plane polarized dipole, we find $\Gamma_{\rightarrow}/\Gamma_{ND} = 4.7$. The collection efficiency by a 1.49 NA objective is $\beta_{\rightarrow}^{1.49} = 36\%$. For an out-of-plane polarized dipole we find $\Gamma_{\uparrow}/\Gamma_{ND} = 5.3$ and $\beta_{\uparrow}^{1.49} = 32\%$. Simple averaging over dipole orientation probability (2/3 for in-plane vs 1/3 for out-of-plane) and collection efficiency yields $\Gamma_{ave}/\Gamma_{ND} = 4.9$. In the experiment, the average lifetime for NVEs found on sapphire is 20 ns, corresponding to $\Gamma_{tot}/\Gamma_{ND} = 8.5$. By comparing the average theoretical and experimental decay rates, we estimate that the quantum yield of such NVE is 22% and

$\Gamma_{nr}/\Gamma_{ND} = 3.6$. An accurate measurement of quantum yield requires measuring single NV centers and a highly controlled modification of the density of states.

c. Nanodiamond on a TiN substrate immersed in oil

For an in-plane polarized dipole, we find $\Gamma_{\rightarrow}/\Gamma_{ND} = 11$ and $\beta_{\rightarrow}^{1.49} = 35\%$. For an out-of-plane polarized dipole, we find $\Gamma_{\uparrow}/\Gamma_{ND} = 40$ and $\beta_{\uparrow}^{1.49} = 10\%$. The decay rate averaged over polarization and collection efficiency is $\Gamma_{ave}/\Gamma_{ND} = 15$. Experimentally, the average lifetime found on TiN is 9.5 ns, corresponding to $\Gamma_{tot}/\Gamma_{ND} = 17.9$. Substracting, we find $\Gamma_{nr}/\Gamma_{ND} = 2.9$, which agrees well with the value found for NVEs on TiN. We conclude that the observed lifetime change between the NVEs on sapphire and TiN substrates can be explained by the presence of SPP modes at the TiN/immersion oil interface. We note that in both cases of plasmonic and dielectric substrates, the difference between the expected and observe lifetime can be explained by similar rates of nonradiative decay.

8. ODMR contrast

In addition to the C_{T1} contrast, we have examined the optically detected magnetic resonance (ODMR) strength of the NVEs. In this scheme, the contrast was measured under constant optical excitation by modulating the resonant microwave field around 2.87 GHz to transfer a fraction of the optically initialized spin population to the $m_s = \pm 1$ subsystems. We have recorded the ODMR spectra (see Supplementary Figure 8(a)) and studied the peak contrast as a function of the NVE fluorescence lifetime.

We found that, similarly to the C_{T1} contrast, the ODMR contrast is correlated with the fluorescence lifetime (see Supplementary Figure 8(b)). However, there exists a wide spread of recorded ODMR values for a given lifetime. This dispersion may result from the microwave wire's gradient magnetic field and subsequent variation in field strength among different nanodiamonds. We also note a strong energy splitting of the $m_s = \pm 1$ states, indicating high levels of strain inside the nanodiamonds, possibly caused by a high impurity concentration.

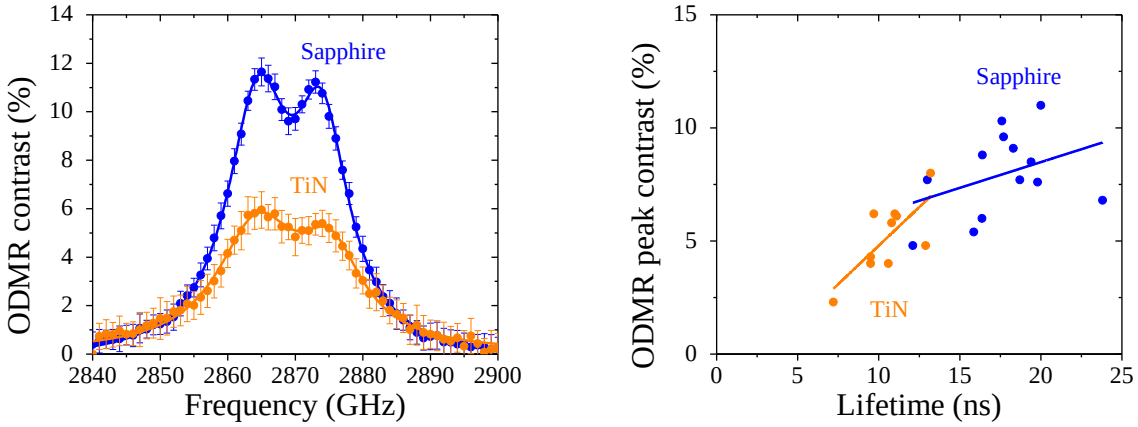

Supplementary Figure 8. (a) Typical ODMR spectra of NVEs found on sapphire and TiN. (b) Average of the two ODMR contrast peaks for each NVE as a function of NVE lifetime. Linear fits are provided for reference.

9. Decrease of C_{T1} at high optical powers

At optical powers, corresponding to $k_{opt} > 2$ MHz, we observed a decrease in C_{T1} (see Supplementary Figure 9). A small decrease of spin contrast is expected at high powers from the kinetic model described in the main text. As the spin initialization starts to occur faster than the duration of the detection window, the fluorescence from the remainder of the detection window becomes identical for the two spin subsystems, thus reducing the spin contrast. Also, two-photon induced ionization occurs at powers beyond optical saturation, leading to the loss of spin information and spin contrast. However, the observed decrease of C_{T1} with laser power is much steeper than the kinetic theory predicts and what is expected from the ionization of individual NV centers.

We have not yet found a rigorous quantitative explanation for the observed decrease in contrast. Here, we fit the contrast dependence on laser power using the following phenomenological expression for the thermalized spin photon counts:

$$\tilde{N}_{\infty}(k_{opt}) = N_{\infty} + (N_0 - N_{\infty})\left(1 - e^{-k_{opt}/k_0}\right) \quad \text{(S5)}$$

In this expression, N_0 and N_{∞} are the photon counts from the initialized and fully thermalized spins, respectively, given by the kinetic theory. $\tilde{N}_{\infty}(k_{opt})$ is the phenomenologically modified photon count from the thermalized spin and k_0 was fitted to be around 30 MHz.

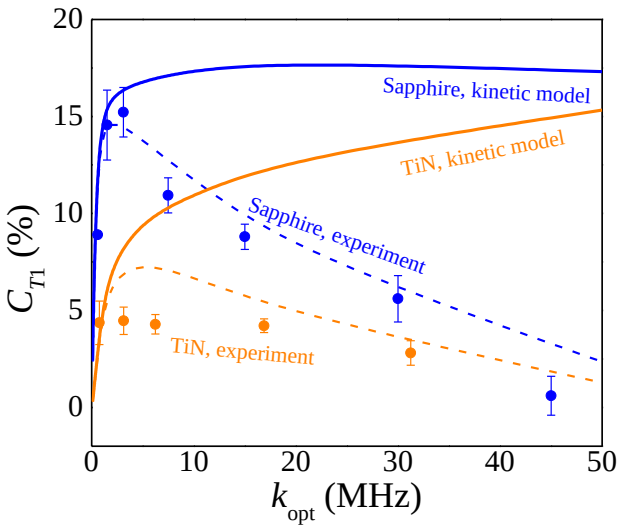

Supplementary Figure 9. Dependences of C_{T1} on optical power for NVEs on sapphire and TiN show a decrease at high powers. The dependences are fitted (the dashed lines) using a phenomenological spin polarization term.

10. **Spin non-conserving transitions**

In Ref [S4] it was shown that spin non-conserving transitions (SNCTs) can play a determining role in the dependence of spin contrast on power. The authors assumed that SNCTs account for 2 percent of the radiative decays and pump absorption events. In their model, the spin readout SNR is negatively affected by moderate Purcell effect ($F_P > 2$) even for single NVs at high pump powers. However, it is currently understood that the SNCTs can only arise from the hyperfine interactions in the NV excited orbital state [S5] and their probability per optical excitation cycle is on the order of 10^{-3}. With such probability of radiative spin mixing, the Purcell enhancement's benefit for NVs with short lifetimes would be limited. However, it still could be significant compared to the unenhanced case.

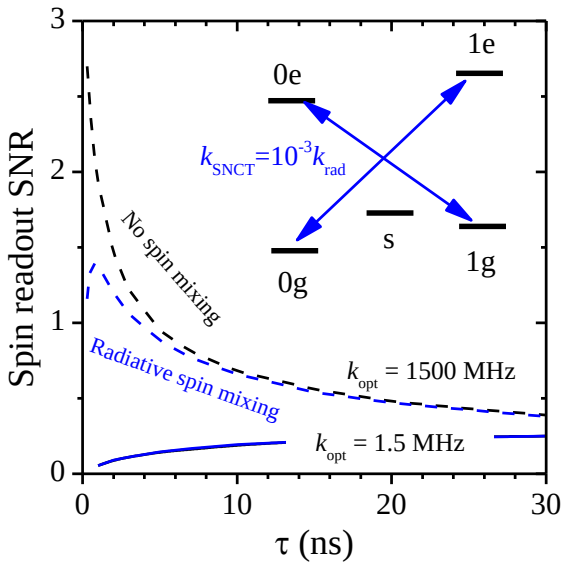

Supplementary Figure 10. Influence of spin non-conserving transitions (shown in inset with blue arrows) on the spin readout SNR for a single NV center for weak optical excitation (solid) and at optical saturation (dashed). At saturation, the effect of SNCTs (blue curves) plays a role only at small lifetimes.

In Supplementary Figure 10 we plot the spin readout SNR for two kinetic models. The first model is described in the main text and does not consider the SNCTs (black curves). The second model assumes radiative SNCTs of the form $|0g\rangle \leftrightarrow |1e\rangle$ and $|0e\rangle \leftrightarrow |1g\rangle$, with transition rates $k_{\mathrm{SNCT}} = 10^{-3} k_{\mathrm{rad}}$ (blue curves). In the strong excitation regime, the presence of SNCTs leads to the appearance of an optimal fluorescence lifetime ~ 1 ns for the spin readout SNR.

References

[S1] N. Kinsey, M. Ferrera, G. V Naik, V. E. Babicheva, V. M. Shalaev, and A. Boltasseva, Opt. Express **22**, 12238 (2014).

[S2] D. O'Connor and D. Phillips, *Time-Correlated Single Photon Counting* (Academic Press, London, 1984).

[S3] V. V. Temnov and U. Woggon, Phys. Rev. Lett. **95**, 243602 (2005).

[S4] S. A. Wolf, I. Rosenberg, R. Rapaport, and N. Bar-Gill, Phys. Rev. B **92**, 235410 (2015).

[S5] J. R. Maze, Quantum Manipulation of Nitrogen-Vacancy Centers in Diamond: From Basic Properties to Applications, 2010.